

pubs.acs.org/NanoLett Letter

# Enhanced Coloration Efficiency of Electrochromic Tungsten Oxide Nanorods by Site Selective Occupation of Sodium Ions

Sungyeon Heo, Clayton J. Dahlman, Corey M. Staller, Taizhi Jiang, Andrei Dolocan, Brian A. Korgel, and Delia J. Milliron\*



Cite This: Nano Lett. 2020, 20, 2072-2079



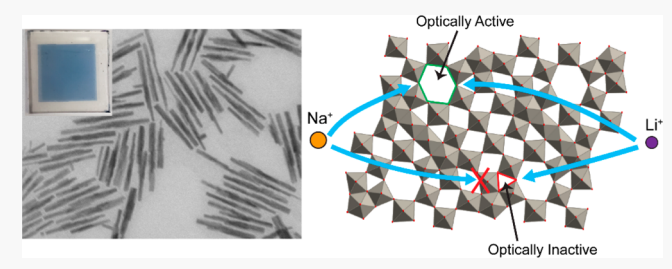
**ACCESS** 

Metrics & More

Article Recommendations

s Supporting Information

**ABSTRACT:** Coloration efficiency is an important figure of merit in electrochromic windows. Though it is thought to be an intrinsic material property, we tune optical modulation by effective utilization of ion intercalation sites. Specifically, we enhance the coloration efficiency of m-WO<sub>2.72</sub> nanocrystal films by selectively intercalating sodium ions into optically active hexagonal sites. To accurately measure coloration efficiencies, significant degradation during cycling is mitigated by introducing atomic-layer-deposited Al<sub>2</sub>O<sub>3</sub> layers. Galvanostatic spectroscopic measurement shows that



the site-selective intercalation of sodium ions in hexagonal tunnels enhances the coloration efficiency compared to a nonselective lithium ion-based electrolyte. Electrochemical rate analysis shows insertion of sodium ions to be capacitive-like, another indication of occupying hexagonal sites. Our results emphasize the importance of different site occupation on spectroelectrochemical properties, which can be used for designing materials and selecting electrolytes for enhanced electrochromic performance. In this context, we suggest sodium ion-based electrolytes hold unrealized potential for tungsten oxide electrochromic applications.

**KEYWORDS:** electrochromism, tungsten oxide, atomic layer deposition, sodium electrolyte

lectrochromic windows made from plasmonic nanocrystals with fast switching speeds, flexible form factors, and selective control over visible and near-infrared transmittance hold promise to reduce energy consumption for heating, cooling, and lighting. 1-8 Practical applications of electrochromic windows require improvements in durability and switching speed. The coloration efficiency (CE), defined as the change in optical density per injected charge density at a particular wavelength, can be a strong predictor of electrochemical stability and speed. High CE indicates a small amount of charge is needed to achieve a given coloration. Nanostructuring has been demonstrated to increase CE, associated with shorter ion diffusion pathways and higher surface area. 10-12 However, the relationship between crystalline structure and CE is scarcely reported, even for the most studied electrochromic materials that exhibit intercalation upon electrochromic charging such as tungsten oxide.<sup>13</sup>

Tungsten oxide is a popular electrochromic material that has achieved initial commercial success because it strongly absorbs visible and near-infrared light in its darkened state. Thus, it can effectively control glare and solar heat gain. <sup>14,15</sup> The crystal structure of WO<sub>3</sub> is analogous to a disordered perovskite structure lacking an A-site species and is monoclinic at room temperature. A continuum of distorted structures forms in substoichiometric Magnéli phases of WO<sub>3-x</sub> with different corner-, edge-, and face-sharing octahedral arrangements due to the crystal shear mechanism. <sup>16</sup> The arrangement of WO<sub>6</sub>

octahedra in the substoichiometric tungsten oxide phases forms regular interstitial tunnels with distinct shapes and sizes. For example, monoclinic  $WO_3$  contains smaller, square-shaped interstitial windows while monoclinic  $WO_{2.72}$  contains trigonal, hexagonal, and square-shaped interstitial windows similar to metastable hexagonal  $WO_3$  (h-WO<sub>3</sub>) (Figure 1d and Figure S1).

Interstitial cation insertion induces electrochromic coloration in tungsten oxide phases. Distinct switching behavior has been observed depending on the occupation of interstitial sites with different size, shape, and local environment. Balaji et al. demonstrated cationic occupation of hexagonal tunnels in h-WO<sub>3</sub> causes greater coloration than ion insertion into "optically inactive" trigonal sites. <sup>17</sup> They observed completely reversible optical modulation even when lithium ions were irreversibly trapped in trigonal cavity sites. Evans et al. observed lithium ion insertion prior to optical modulation during electro-optical imaging of single particles of h-WO<sub>3</sub> and attributed this "waiting time" to occupation of optically inactive trigonal sites. <sup>18</sup> Experimental <sup>17,18</sup> and theoretical <sup>19</sup> studies of h-WO<sub>3</sub> indicate that the interstitial sites have

Received: January 5, 2020
Revised: February 8, 2020
Published: February 21, 2020



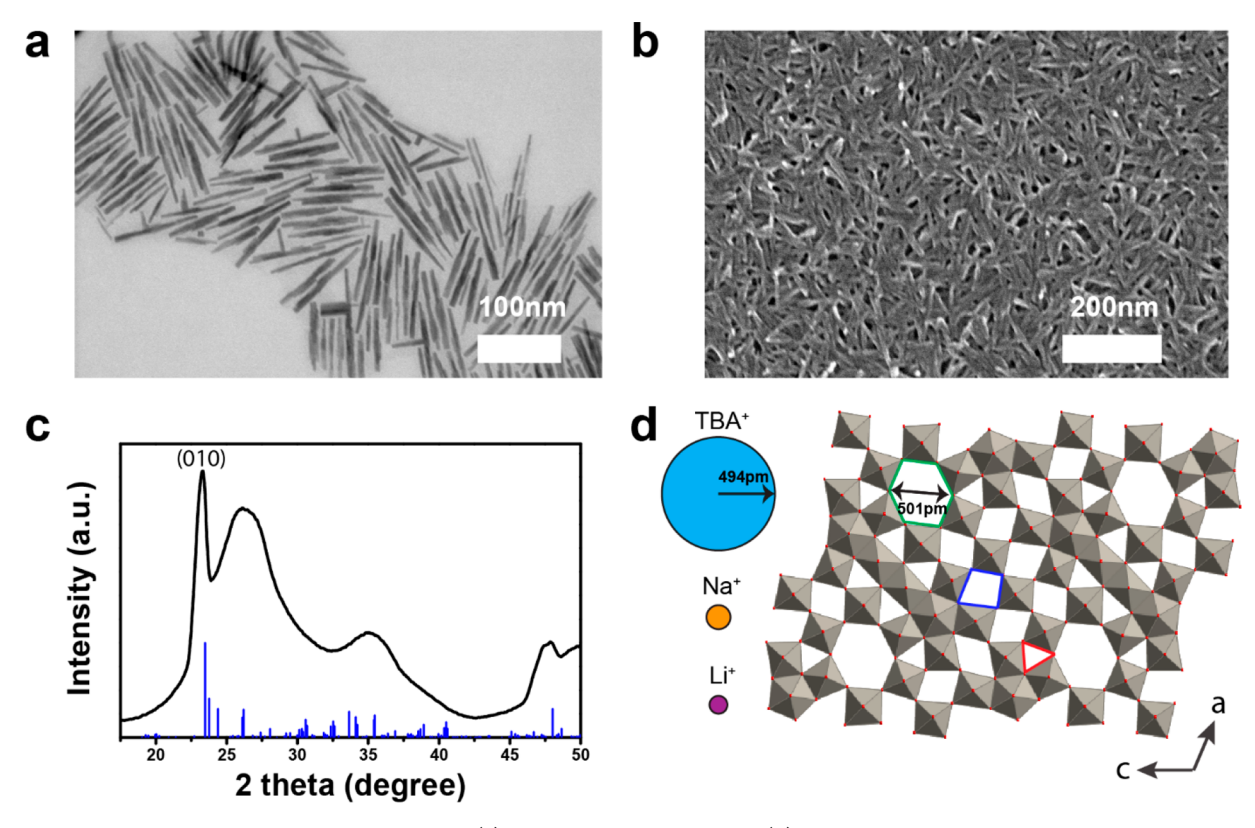


Figure 1. Structural properties of m-WO<sub>2.72</sub> nanorods. (a) STEM image of nanorods. (b) SEM image of porous nanorod film coated with 1 nm  $Al_2O_3$  by ALD. (c) XRD pattern of as-synthesized WO<sub>2.72</sub> nanorods prepared by drop-casting (black) and the corresponding m-WO<sub>2.72</sub> reference pattern (blue, ICSD #15254). (d) Scaled representations of the ionic radii of TBA, sodium, and lithium ions alongside the m-WO<sub>2.72</sub> crystal structure. Different interstitial sites are shown in the (010) plane, including hexagonal tunnels (green), trigonal cavities (red), and square windows (blue).

different optical activities upon ion insertion but a quantitative comparison of CE between each site has not yet been reported.

Monoclinic m-WO<sub>2.72</sub> and hexagonal h-WO<sub>3</sub> each have three distinct interstitial sites: a trigonal cavity with a center-tooxygen distance of 158 pm, a hexagonal site with a closest endto-end distance of 501 pm, and square windows with a closest end-to-end distance of 378 pm (Figure 1d). Lithium ions (radius = 76 pm) are small enough to insert into all three interstitial sites. Hibino et al. calculated the energy of interstitial lithium defects in each of these three sites in h-WO3. Their results suggested that lithium ions will first occupy trigonal cavities, followed by hexagonal tunnels and square windows. 19 However, sodium ions (radius = 102 pm), which are 34% larger than Li ions, cannot fit into trigonal cavities. Interstitial cations in trigonal cavities are not believed to contribute significantly to electrochromic coloration. 17-19 Thus, eliminating these regions as a destination for inserted sodium ions may enhance CE in h-WO3 and m-WO272 by directing cation insertion into optically active hexagonal tunnel

Herein, we demonstrate that nanostructured m-WO $_{2.72}$  exhibits high CE upon charging with a sodium-based electrolyte. Sodium ions can selectively insert into optically active hexagonal tunnel sites, leading to improved CE compared to charging with a nonselective lithium-based electrolyte. Good cycling stability is necessary to compare the electrochromic response and CE between different electrolytes. We show that atomic layer deposition (ALD) of a protective layer  $Al_2O_3$  on m-WO $_{2.72}$  thin films eliminates parasitic side reactions. We find that  $Al_2O_3$ -coated m-WO $_{2.72}$ 

has lower overall electrochromic modulation in sodium-based electrolyte compared to lithium-based electrolyte, but an enhanced CE with a kinetic response that is not significantly limited by ion diffusion. Our results indicate that high-performance electrochromic behavior in nanocrystal tungsten oxide films can be achieved with earth-abundant sodium-based electrolytes.

## ■ RESULTS AND DISCUSSION

1. Colloidal Monoclinic WO<sub>2,72</sub> Nanorods Have Three **Different Interstitial Sites.** A diversity of interstitial sites is observed in both h-WO3 and m-WO2.72 phases, including hexagonal tunnels, square windows, and trigonal cavities. However, colloidal synthesis of metastable h-WO<sub>3</sub> nanocrystals without interstitial dopants such as Cs is challenging.<sup>20</sup> Thus, substoichiometric m-WO<sub>2.72</sub> nanorods were synthesized to compare the electrochromic response of different interstitial sites. High aspect-ratio m-WO $_{2.72}$  nanorods with narrow width  $(7.0 \pm 1.1 \text{ nm})$  and longer length  $(75.5 \pm 15.2 \text{ nm})$  were synthesized as previously described (Figure 1a).21 X-ray diffraction (XRD) shows much narrower (010) peaks compared to other reflections (Figure 1c). Thus, the (010) crystallographic direction is oriented along the longer nanorod axis, similar to previous reports.<sup>21</sup> The high concentration of oxygen-vacancies in m-WO<sub>2.72</sub> is known to induce metallic behavior and to facilitate rapid electrochromic switching due to charge compensation by conduction band free electrons.<sup>22</sup> We expect degenerate m-WO<sub>2.72</sub> nanorods to exhibit localized surface plasmonic resonance (LSPR) owing to their metallicity and confined geometry. Thus, visible and infrared absorption

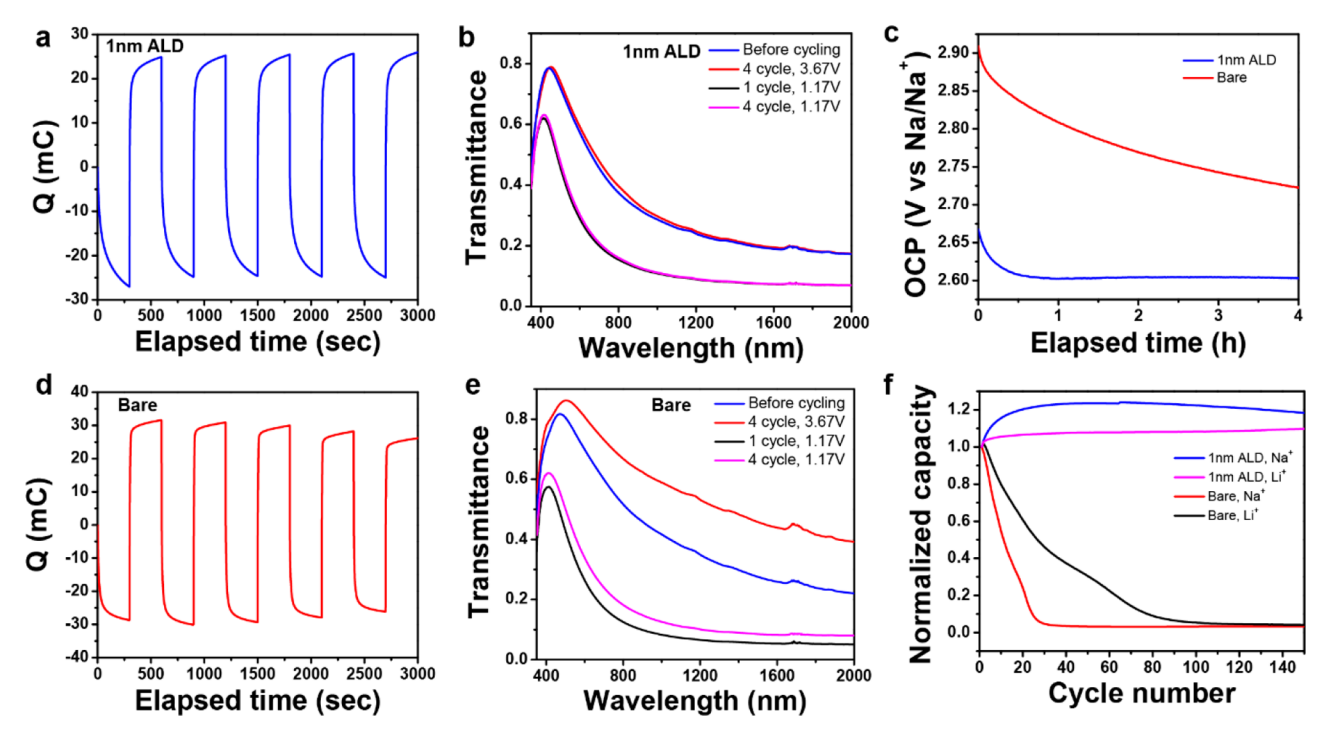


Figure 2. Spectroelectrochemical properties of bare and 1 nm  $Al_2O_3$ -coated m- $WO_{2,72}$  nanorod films. Chronoamperometric cycling between 1.17 and 3.67 V (versus  $Na/Na^+$ ) of (a) 1 nm  $Al_2O_3$ -coated and (d) bare m- $WO_{2,72}$  films. Transmittance spectra of (b) 1 nm  $Al_2O_3$ -coated and (e) bare m- $WO_{2,72}$  films after several cycles. (c) OCP of bare and 1 nm  $Al_2O_3$ -coated m- $WO_{2,72}$  films immersed in 0.5 M  $NaClO_4$  in propylene carbonate electrolytes in dark condition before cycling. (f) Capacity change during chronoamperometric cycling tests with 5 min charging (1.17 V) and discharging (3.67 V) steps of bare and 1 nm  $Al_2O_3$ -coated films in sodium and lithium electrolytes.

are expected to come from the transverse and longitudinal mode of LSPR, respectively. However, broad optical extinction in the visible and infrared may also be partially from polaronic absorption (Figure S2).<sup>22,23</sup>

The crystal structure of m-WO<sub>2.72</sub> has continuous hexagonal tunnels that extend along the b-axis (Figure 1d and Figure S1). Similar continuous hexagonal tunnels in h-WO<sub>3</sub> are believed to enhance proton transport and result in pseudocapacitive charging kinetics. <sup>24,25</sup> We hypothesize that the size of different interstitial sites, including hexagonal tunnels, may induce selective charge transport and optical coloration in m-WO<sub>2.72</sub>, depending on the composition of the electrolyte cations.

Low-temperature processing was used to preserve the crystal structure upon film deposition. Thermal annealing is commonly used to remove the insulating ligands between nanocrystals in a deposited film. However, annealing can change the oxygen vacancy concentration and crystal structure of transition metal oxides such as WO<sub>x</sub> and NbO<sub>x</sub>. In a previous study, Heo et al. instead fabricated electrically conductive thin films by chemically stripping the ligands from colloidal tungsten oxide nanorods before spin-coating. Treatment with Meerwein's salt (Et<sub>3</sub>OBF<sub>4</sub>) to remove ligands also induces electrostatic repulsion between dispersed nanorods enabling room temperature deposition of films that are both porous and electrically conductive. Here, following the same method, conductive thin films of m-WO<sub>2.72</sub> were fabricated by spin-coating ligand-stripped nanorods (Figure S3 and S4). Films retain the strong visible and near-infrared light absorption of dispersed m-WO<sub>2.72</sub> nanorods (Figure 2e) but with spectral broadening that may be caused by optical coupling between particles.2

2. Electrolyte Decomposition Causes Rapid Film Degradation. As-deposited films show poor cycle stability

with either lithium- or sodium-based propylene carbonate (PC) electrolytes. Charge capacity vanishes after about 20 cycles in 0.5 M NaClO<sub>4</sub> in PC and after about 100 cycles in 0.5 M LiClO<sub>4</sub> in PC (Figure 2f). Poor cycle stability limits the practical performance and prevents an accurate quantification of injected charge density for calculations of CE. There are three plausible causes of poor cycle stability in these films: (1) delamination of nanocrystals, (2) electrolyte decomposition at the nanocrystal surface, and (3) irreversible ion trapping within the crystal structure.<sup>28–30</sup> Although several reports have proposed delamination as a source of degradation,<sup>5,31</sup> there is a scarcity of systematic studies relating cycle stability to chemical or structural phenomena in nanocrystalline electrochromic films.

Film delamination is unlikely to explain the poor stability. Even after 400 cycles, well beyond the complete capacity fade of the electrode (Figure 2f), films look pristine to the naked eye. Moreover, cross-sectional SEM imaging of cycled films (400 cycles in 0.5 M NaClO $_4$  in PC electrolyte) shows no evidence of roughening or loss of nanocrystal coverage (Figure S5a).

Ion trapping is also unlikely as a source of degradation in asdeposited m-WO $_{2.72}$  nanorod films. Charge capacity fades to nearly zero upon cycling in the sodium-based electrolyte, but charge capacity should only be impacted by ion insertion into deep-trapping sites. Charge capacity from shallow sites, such as the hexagonal tunnels that favor capacitive sodium insertion, should not show capacity fade from ion trapping. We note that the origin of degradation in these nanocrystalline thin films is strikingly different from dense tungsten oxide films, where electrochromic cycle fade is attributed mainly to ion trapping.  $^{32}$ 

We suspected electrolyte degradation as the primary cause of degradation. As-deposited nanorod films show a continuous decrease in open-circuit potential (OCP) upon immersion in 0.5 M NaClO<sub>4</sub> in PC electrolyte, even before electrochemical cycling. A similar phenomenon was observed for LiMn<sub>2</sub>O<sub>4</sub> thin films immediately after exposure to lithium-based electrolytes and was attributed to the spontaneous formation of a solid electrolyte interphase (SEI).<sup>33</sup> The high internal surface area of nanocrystalline films may increase surface reaction rates with the electrolyte. Despite shorter path lengths for ion diffusion, enhanced SEI formation impedes ion transport and limits their practical application in batteries. 34,35 The potential range usually used for electrochromic cycling (1.5-4 V versus Li/ Li<sup>+</sup>) is moderate compared to battery operation (0-4 V versus Li/Li<sup>+</sup>). Lithium and sodium-based alkylcarbonate electrolytes typically breakdown only at potentials below 1.5 V versus Li/ Li<sup>+</sup>, and electrochromic cycling with, for instance, tin-doped In<sub>2</sub>O<sub>3</sub> nanocrystalline thin films shows robust electrochromic cycle stability.<sup>36</sup> Therefore, the composition of m-WO<sub>2.72</sub> nanorods in particular is likely responsible for the degradation. Indeed, oxygen-deficient tungsten oxide nanowires show high electrochemical catalytic activity.<sup>37</sup> Degradation is much more pronounced in the sodium electrolyte compared to the lithium electrolyte (Figure 2f). Therefore, a combination of the electrode material properties and electrolyte composition causes poor stability in m-WO $_{2.72}$  films, consistent with many examples from the battery field.  $^{38,39}$ 

**3.** ALD of  $Al_2O_3$  Forms a Protective Coating. Protective oxide coatings, applied by ALD, have been employed in the battery field to prevent electrolyte decomposition and mechanical delamination. Thin ALD-coated oxide barriers can also prevent parasitic photochromic responses in electrochromic materials exposed to continuous irradiation. Wang et al. employed ALD-coated  $Ta_2O_5$  as a hole-blocking layer to reduce photochromic responses in nanocrystalline tungsten oxide films. ALD of  $Al_2O_3$ , which has a larger bandgap (7.1 eV) than  $Ta_2O_5$  (3.8 eV), can effectively block hole transfer to the electrolyte.  $Al_2O_3$  is also optically passive, allowing us to study modulation properties of  $Al_2O_3$ -coated tungsten oxide materials.

As-deposited m-WO<sub>2.72</sub> films were coated with Al<sub>2</sub>O<sub>3</sub> by ALD. XPS measurements show an increase in both the Al 2p peak and Al<sub>2</sub>O<sub>3</sub>-related O 1s peak upon deposition of 1 or 2 nm of Al<sub>2</sub>O<sub>3</sub> by ALD (Figure S6). XRD measurements of the Al<sub>2</sub>O<sub>3</sub>-coated films demonstrate the crystal phase of m-WO<sub>2.72</sub> was retained after ALD (Figure S3). A slight decrease in optical transmittance was observed (Figure S7), likely due to the chemically reducing atmosphere present during ALD.<sup>46</sup>

ALD coating of a 1 nm Al<sub>2</sub>O<sub>3</sub> layer improves the OCP and cycling stability of m-WO<sub>2.72</sub> nanorod films (Figure 2c,f). An initial capacity fade occurs upon the first charge cycle, perhaps due to the activation of Al—O—Na bonding as reported in a previous study.<sup>41</sup> After the first cycle, Al<sub>2</sub>O<sub>3</sub>-coated films show robust charging and optical modulation stability even after 100 cycles in a sodium-based electrolyte (Figure 2b,e). Films coated with a thicker 2 nm Al<sub>2</sub>O<sub>3</sub> layer show a gradual increase in charge capacity during the first 10 cycles (Figure S8).

 $Al_2O_3$  passivation allows the confirmation of our hypothesis that delamination is not a significant source of capacity fade in m-WO<sub>2.72</sub> nanorod films. Cross-sectional SEM measurements of bare and 1 nm  $Al_2O_3$ -coated films after 400 cycles reveal similar roughness and thickness (Figure S5). Therefore, the

stabilizing effects of ALD are not due to improvements in mechanical robustness.

To determine if electrolyte decomposition is the primary source of capacity fade, we employed time-of-flight secondaryion mass spectrometry (TOF-SIMS) to examine the compositional profile of the films after cycling. This technique has been employed in the battery field to investigate the reactivity of electrode-electrolyte interfaces with ultrahigh selectivity and sensitivity. 47-49 TOF-SIMS depth profiling was applied to both as-deposited and 1 nm Al<sub>2</sub>O<sub>3</sub>-coated films after 30 cycles in 0.5 M NaClO<sub>4</sub> in tetraglyme (Figure S9). The analysis confirms Al<sub>2</sub>O<sub>3</sub> is deposited throughout the entire film upon ALD, evidenced by the complete penetration of the Al- and AlWO<sub>5</sub><sup>-</sup> signals in the Al<sub>2</sub>O<sub>3</sub> coated film (Figure S9). Degradation products of tetraglyme and NaClO<sub>4</sub>, represented by related secondary ions such as C<sub>2</sub>HO<sup>-</sup> and Cl<sup>-</sup>, respectively, are much more prevalent in the as-deposited m-WO<sub>2.72</sub> films compared to the Al<sub>2</sub>O<sub>3</sub>-coated films. Both films show similar sodium ion depth profiles, indicating complete penetration of the electrolyte into the film; however, the bare film has higher sodium ion content. Byproducts of electrolyte degradation at the nanocrystal surface are expected to inhibit ion transport through the film. The Al<sub>2</sub>O<sub>3</sub> film effectively reduces electrolyte degradation and subsequent deposition of degraded species at the nanocrystal surface.

Electrochemical impedance spectroscopy (EIS) measurements confirm charge cycling of uncoated films leads to poorer charge transport. Bare m-WO<sub>2.72</sub> films, both before and after cycling, were tested at 1.46 V (versus Na/Na<sup>+</sup>). Nyquist plots were fitted with a Randles circuit model (Figure S10). The high-frequency region is related to the series resistance, the intermediate frequency region is related to the charge transfer resistance, and the low frequency region is related to the Warburg diffusion element ( $Z_{\rm w}$ ). Substantial increases in both the charge transfer resistance (42 to 178  $\Omega$ ) and Warburg diffusion impedance (43 to 8107  $\Omega$ ) occurred after cycling the bare m-WO<sub>2.72</sub> nanorod film. Thus, electrolyte degradation diminishes charge transfer and ion diffusion across the uncoated nanocrystal surface.

The passivating effects of Al<sub>2</sub>O<sub>3</sub> ALD are further confirmed by measuring photochromism upon exposure to UV light, which can limit the practical performance of smart windows. As-deposited nanorod films in contact with electrolyte show optical coloration upon exposure to UV-radiation (365 nm) for 3 h (Figure S7). This coloration occurs across the visible and near-IR and broadly overlaps the electrochromic modulation observed during electrochemical reduction (Figure 2). The photochromic effect in tungsten oxide is attributed to photogenerated holes that transfer to the electrolyte, while electrolyte breakdown forms protons and electrons that are transferred to the electrode. ALD-coated films show only slight changes in transmittance upon UV irradiation (Figure S7). Thus, Al<sub>2</sub>O<sub>3</sub> can effectively block photogenerated hole transfer from m-WO<sub>2.72</sub> to the electrolyte.

4. Spectroelectrochemical Modulation Is Sensitive to the Electrolyte Cation. The cycle stability of 1 nm  $\rm Al_2O_3$ -coated m-WO<sub>2.72</sub> nanorod films is sufficient to compare electrochromic responses between electrolytes. To this end, we tested electrolytes with three different sized monovalent cations: lithium, sodium, and tetrabutylammonium (TBA) ions.

The crystal structure of m-WO<sub>2.72</sub> (Figure 1d) contains three distinct interstitial sites, namely hexagonal tunnels,

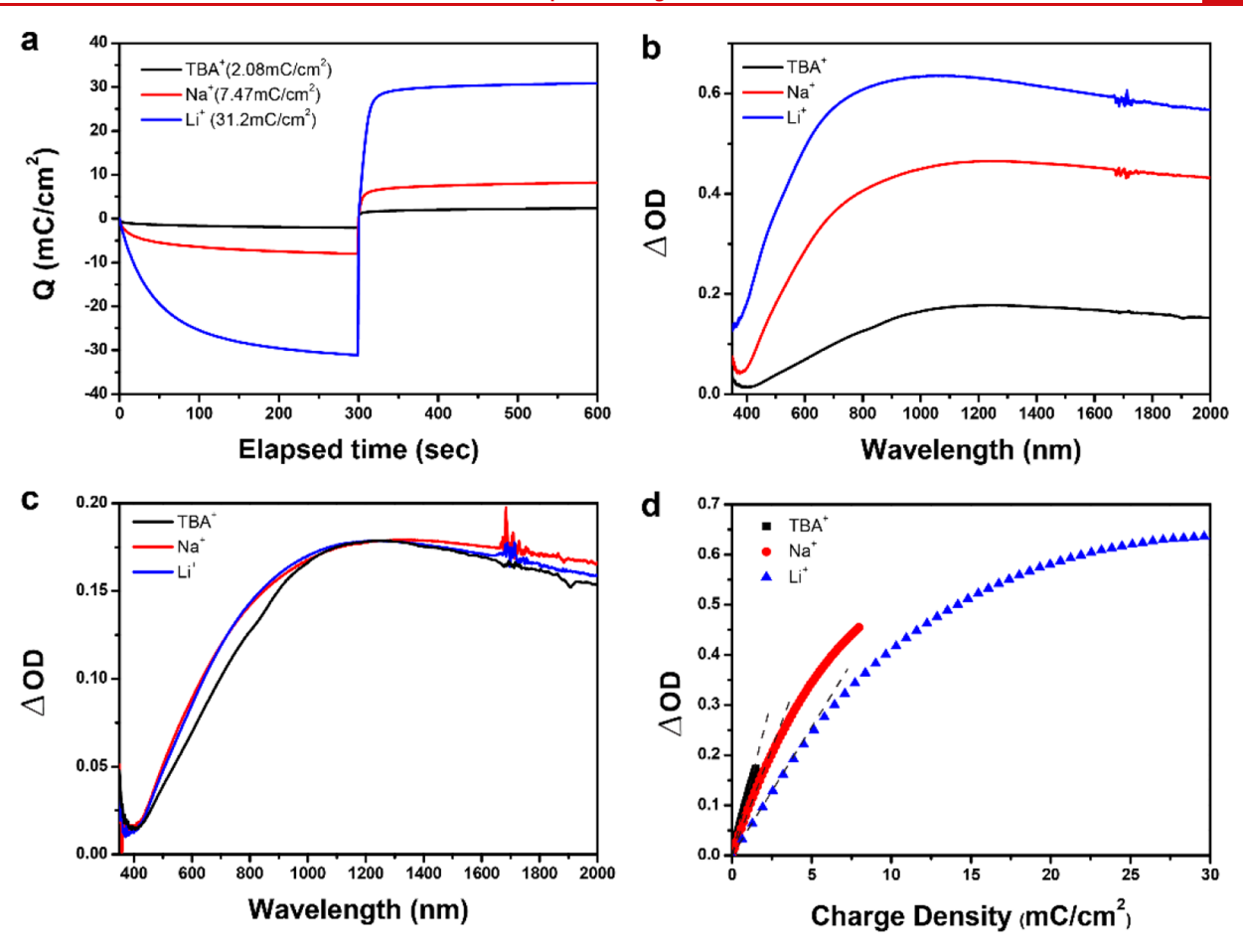


Figure 3. Spectroelectrochemical properties of 1 nm  $Al_2O_3$ -coated m-WO<sub>2.72</sub> nanorod films with different electrolyte cations. (a) Chronoamperometric charging and discharging with sodium, lithium, and TBA electrolytes with similar applied potentials (1.2 V from each OCP). (b) Optical density modulation after the electrochemical reduction step shown in (a). (c) Modulation in optical density, collected at a different state of charge to reach the same peak optical density. (d) Optical density modulation at 1200 nm plotted against accumulated galvanostatic charge density for 1 nm  $Al_2O_3$ -coated m-WO<sub>2.72</sub> films with different electrolytes. Similar potentials (1.2 V from each OCP) were applied.

square windows, and trigonal cavities. TBA is too large (radius = 494 pm) to fit in any interstitial sites and is expected to contribute only double-layer capacitive charge compensation at the nanorod surface. Lithium (radius = 76 pm) and sodium (radius = 102 pm) ions can both insert into hexagonal tunnels. However, only lithium can enter trigonal cavities (center-tooxygen distance = 158 pm) by passing through hexagonal tunnels and square windows sequentially. Previous experimental and theoretical studies have asserted that lithium occupancy follows a sequential order based on energetic stability proceeding from trigonal cavities to hexagonal tunnels and finally to square windows. Sodium is too large to occupy trigonal cavities or square windows, and earlier studies have shown sodium ions to preferentially occupy larger hexagonal or pentagonal sites in substoichiometric tungsten oxide. 51,52 Thus, we expect that the different occupancy and local environment of lithium, sodium, and TBA ions will impact electrochromic behavior in m-WO<sub>2,72</sub> nanorod films.

Charge capacity and electrochromic modulation range of  ${\rm Al_2O_3}$ -coated m-WO $_{2.72}$  films trend inversely with the electrolyte cation size. A consistent reducing potential from the OCP of the uncharged ALD-coated film (1.2 V from each OCP) was applied for each electrolyte. The capacity of films charged using the largest cation, TBA (2 mC/cm²) is an order of magnitude lower than the capacity with the smallest cation,

lithium (31 mC/cm²). The low capacity with TBA is unsurprising, considering that TBA is too large to insert into m-WO<sub>2.72</sub> and can only contribute to double-layer capacitive charging. The characteristic rectangular shape of cyclic voltammetry (CV) measurements with TBA confirms this capacitive charging behavior (Figure S11). Sodium, which has an intermediate radius, yields a capacity of 7 mC/cm² (Figure 3a). Optical modulation also follows this trend with smaller cations inducing greater electrochromic coloration (Figure 3b). The increased optical modulation and charge capacity of sodium compared to TBA indicate that it may insert into the m-WO<sub>2.72</sub> crystal structure but to a lesser extent than lithium.

The optical modulation per unit charge (i.e., CE) is greater for sodium ions than lithium ions, as shown in Figure 3d. The lower absolute charge capacity and modulation in a sodium-based electrolyte is a consequence of the sodium ion's large size that precludes insertion into trigonal cavities or square windows. Instead, sodium ions occupy hexagonal tunnels upon insertion. Balaji et al. demonstrated that coloration in lithiated tungsten oxide is dominated by lithium occupation of hexagonal tunnels and square windows sites, not trigonal cavities. To, sodium ion insertion favors more optically active sites, whereas lithium occupies both optically active (hexagonal) and inactive (trigonal) sites upon insertion.

Indeed, we find a significantly greater CE upon charging with sodium  $(81 \text{ cm}^2/\text{C})$  compared to lithium  $(49 \text{ cm}^2/\text{C})$ .

The different charge densities measured for sodium and lithium insertion are consistent with the ratio of crystallographic interstitial sites in m-WO<sub>2.72</sub>. If each cation selectively occupies different interstitial sites, the ratio of charge densities should match the number density ratio between crystallographic sites. Figure S12 compares the number ratio of trigonal cavities and hexagonal sites using both geometric and charge density calculations. Two assumptions were employed for this comparison. First, we assumed lithium ions do not occupy the square windows in our moderate potential window (within 2.5 V from the most oxidizing potential). 17 Second, we assumed complete occupation of accessible sites (hexagonal sites for sodium; hexagonal and trigonal sites for lithium) after charging. Hexagonal tunnel occupation was estimated by subtracting double-layer capacitance, calculated from charge capacity with TBA, from the total sodium ion charge capacity. Trigonal cavity density was calculated by subtracting the total sodium charge capacity from the total lithium charge capacity. The number ratio between trigonal cavities and hexagonal tunnels is roughly the same between geometric and charge density approximations for m-WO<sub>2.72</sub> (Figure S12), supporting our site-selective model.

Ion insertion and double-layer capacitance cause distinct electrochromic responses in m-WO<sub>2,72</sub>. Figure 3c compares the spectral line shape for the modulation for each cation. The smaller inserting cations, sodium and lithium ions, induce greater visible to near-infrared coloration (500–900 nm) upon electrochemical reduction than TBA ions. Visible and infrared absorption in crystalline tungsten oxide is caused by either Drude responses of free carriers or polaron absorption, depending on the particular crystal phase, temperature, and doping.<sup>23,53-55</sup> Absorption due to polaron or interband defect states arising from self-trapped carriers in m-WO<sub>2.72</sub> can manifest as higher-energy absorption features (>1.5 eV or wavelength <900 nm). <sup>23,56</sup> Inserted ions impact the local structure, polarizability, and phonon interactions that generate localized polarons. Ion insertion can therefore change the spectrum or intensity of polaronic optical interactions in the visible range, more so than carriers introduced by purely capacitive charging which involves less perturbation to the crystal. Thus, electrochromic m-WO<sub>2.72</sub> appears to be sensitive to distinct charging processes from capacitance (TBA ions) and ion insertion (lithium or sodium ions), analogous to such differences reported in nanocrystalline anatase TiO2.

Site occupation by different ions affects not only optical modulation but also electrochemical properties. Charge storage kinetics can be derived from CV measurements at different scan rates. The measured current can be modeled as a convolution of capacitive-like and diffusion-limited processes according to the following equation:  $I(V) = k_1 \nu$  (capacitive) +  $k_2 \nu^{1/2}$  (diffusion-controlled). <sup>57,58</sup>

The non-diffusion-limited contribution to charge capacity at a particular potential can be calculated from  $k_1$  by fitting the current at different scan rates (Figure S13). This capacitive-like contribution with a sodium-based electrolyte is as high as 92% (Figure 4). We attribute this to both the high surface-to-volume ratio in porous nanocrystalline films and the large size of intracrystalline hexagonal tunnels. Our results contrast previous studies of aqueous sodium electrolytes, which concluded that sodium ions cannot traverse hexagonal tunnels. <sup>24</sup> Rather, we observe rapid sodium diffusion through

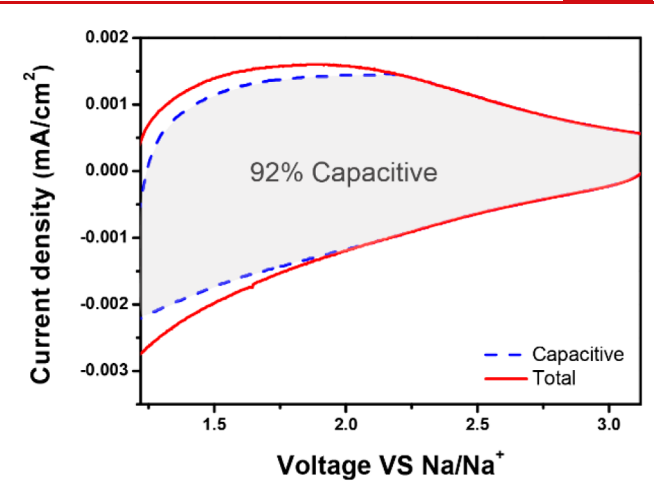


**Figure 4.** Voltammetric response (1 mV/s) of a 1 nm  $Al_2O_3$ -coated m-WO<sub>2,72</sub> nanorod film with a sodium-based electrolyte. The capacitive contribution to charge capacity, determined by kinetic rate analysis, is shaded.

m-WO $_{2.72}$  nanorods. It is possible that the difference is related to the ease of desolvating propylene carbonate as compared to water.

In summary, we have demonstrated that effective utilization of different interstitial cavity sites in substoichiometric m-WO<sub>2.72</sub> can be used to enhance CE in electrochromic nanocrystal films. A robust, fast-switching and cyclable electrochromic film was prepared by spin coating ligandstripped colloidal m-WO<sub>2.72</sub> nanorods and using ALD to apply a protective 1 nm Al<sub>2</sub>O<sub>3</sub> coating. The passivating layer prevents the rapid degradation of electrolytes during cycling and allows for a quantitative comparison of the electrochromic performance using different electrolyte systems. Sodium electrolytes are found to exhibit enhanced CE by selectively inserting ions into optically active hexagonal tunnel sites through a capacitive charging process. More broadly, our results demonstrate the importance of understanding the precise local structure for ion occupation in ion-insertion electrodes for electrochromic materials.

# ASSOCIATED CONTENT

#### Supporting Information

The Supporting Information is available free of charge at https://pubs.acs.org/doi/10.1021/acs.nanolett.0c00052.

Experimental and characterization details, UV-visible-NIR, XRD, TOF-SIMS, SEM, XPS, transmittance, EIS, chronoamperometric cycling, and cyclic voltammetry data (PDF)

## AUTHOR INFORMATION

#### **Corresponding Author**

Delia J. Milliron — McKetta Department of Chemical Engineering, The University of Texas at Austin, Austin, Texas 78712, United States; orcid.org/0000-0002-8737-451X; Email: milliron@che.utexas.edu

### Authors

Sungyeon Heo − McKetta Department of Chemical Engineering, The University of Texas at Austin, Austin, Texas 78712, United States; © orcid.org/0000-0001-8690-5748

- Clayton J. Dahlman McKetta Department of Chemical Engineering, The University of Texas at Austin, Austin, Texas 78712, United States; orcid.org/0000-0002-4555-4846
- Corey M. Staller McKetta Department of Chemical Engineering, The University of Texas at Austin, Austin, Texas 78712, United States; orcid.org/0000-0001-8665-2840
- **Taizhi Jiang** McKetta Department of Chemical Engineering, The University of Texas at Austin, Austin, Texas 78712, United States; ⊚ orcid.org/0000-0003-1995-6187
- Andrei Dolocan Texas Materials Institute, The University of Texas at Austin, Austin, Texas 78712, United States;
  ocid.org/0000-0001-5653-0439
- Brian A. Korgel McKetta Department of Chemical Engineering, The University of Texas at Austin, Austin, Texas 78712, United States; orcid.org/0000-0001-6242-7526

Complete contact information is available at: https://pubs.acs.org/10.1021/acs.nanolett.0c00052

#### **Notes**

The authors declare the following competing financial interest(s): D.J.M. has a financial interest in Heliotrope Technologies, a company pursuing commercial development of electrochromic devices.

#### ACKNOWLEDGMENTS

S.H. and D.J.M. acknowledge funding from CBMM and the Welch Foundation (F-1848). Support was also provided by the National Science Foundation, including NASCENT, an NSF ERC (EEC-1160494, C.M.S.) and CHE-1905263 (C.J.D.). T.J. and B.A.K. acknowledge the funding by the Robert A. Welch Foundation (Grant F-1464) and the Center for Dynamics and Control of Materials (CDCM) supported by NSF Award No. DMR-1720595. ALD was performed at the Center for Electrochemistry at UT Austin. We also acknowledge the NSF Grant DMR-0923096 used to purchase the TOF-SIMS instrument at Texas Materials Institute, UT Austin.

## REFERENCES

- (1) Dahlman, C. J.; Tan, Y.; Marcus, M. A.; Milliron, D. J. Spectroelectrochemical Signatures of Capacitive Charging and Ion Insertion in Doped Anatase Titania Nanocrystals. *J. Am. Chem. Soc.* **2015**, *137*, 9160–9166.
- (2) Cao, S.; Zhang, S.; Zhang, T.; Lee, J. Y. Fluoride-Assisted Synthesis of Plasmonic Colloidal Ta-Doped TiO<sub>2</sub> Nanocrystals for Near-Infrared and Visible-Light Selective Electrochromic Modulation. *Chem. Mater.* **2018**, *30*, 4838–4846.
- (3) Barawi, M.; De Trizio, L.; Giannuzzi, R.; Veramonti, G.; Manna, L.; Manca, M. Dual Band Electrochromic Devices Based on Nb-Doped TiO<sub>2</sub> Nanocrystalline Electrodes. ACS Nano 2017, 11, 3576–3584
- (4) Wang, Y.; Runnerstrom, E. L.; Milliron, D. J. Switchable Materials for Smart Windows. *Annu. Rev. Chem. Biomol. Eng.* **2016**, *7*, 283–304
- (5) Kim, J.; Ong, G. K.; Wang, Y.; LeBlanc, G.; Williams, T. E.; Mattox, T. M.; Helms, B. A.; Milliron, D. J. Nanocomposite Architecture for Rapid, Spectrally-Selective Electrochromic Modulation of Solar Transmittance. *Nano Lett.* **2015**, *15*, 5574–5579.
- (6) Heo, S.; Kim, J.; Ong, G. K.; Milliron, D. J. Template-Free Mesoporous Electrochromic Films on Flexible Substrates from Tungsten Oxide Nanorods. *Nano Lett.* **2017**, *17*, 5756–5761.
- (7) Barile, C. J.; Slotcavage, D. J.; McGehee, M. D. Polymer–Nanoparticle Electrochromic Materials That Selectively Modulate Visible and Near-Infrared Light. *Chem. Mater.* **2016**, 28, 1439–1445. (8) Gu, H.; Guo, C.; Zhang, S.; Bi, L.; Li, T.; Sun, T.; Liu, S. Highly Efficient, Near-Infrared and Visible Light Modulated Electrochromic

- Devices Based on Polyoxometalates and W<sub>18</sub>O<sub>49</sub> Nanowires. ACS Nano **2018**, 12, 559-567.
- (9) Runnerstrom, E. L.; Llordés, A.; Lounis, S. D.; Milliron, D. J. Nanostructured Electrochromic Smart Windows: Traditional Materials and NIR-Selective Plasmonic Nanocrystals. *Chem. Commun.* **2014**, *50*, 10555–10572.
- (10) Lee, S.-H.; Deshpande, R.; Parilla, P. A.; Jones, K. M.; To, B.; Mahan, A. H.; Dillon, A. C. Crystalline WO<sub>3</sub> Nanoparticles for Highly Improved Electrochromic Applications. *Adv. Mater.* **2006**, *18*, 763–766.
- (11) Scherer, M. R. J.; Steiner, U. Efficient Electrochromic Devices Made from 3D Nanotubular Gyroid Networks. *Nano Lett.* **2013**, *13*, 3005–3010.
- (12) Williams, T. E.; Chang, C. M.; Rosen, E. L.; Garcia, G.; Runnerstrom, E. L.; Williams, B. L.; Koo, B.; Buonsanti, R.; Milliron, D. J.; Helms, B. A. NIR-Selective Electrochromic Heteromaterial Frameworks: A Platform to Understand Mesoscale Transport Phenomena in Solid-State Electrochemical Devices. *J. Mater. Chem. C* 2014, 2, 3328–3335.
- (13) Wang, Z.; Zhang, Q.; Cong, S.; Chen, Z.; Zhao, J.; Yang, M.; Zheng, Z.; Zeng, S.; Yang, X.; Geng, F.; Zhao, Z. Using Intrinsic Intracrystalline Tunnels for Near-Infrared and Visible-Light Selective Electrochromic Modulation. *Adv. Opt. Mater.* **2017**, *5*, 1700194.
- (14) Yang, L.; Ge, D.; Zhao, J.; Ding, Y.; Kong, X.; Li, Y. Improved Electrochromic Performance of Ordered Macroporous Tungsten Oxide Films for IR Electrochromic Device. *Sol. Energy Mater. Sol. Cells* **2012**, *100*, 251–257.
- (15) Granqvist, C. G. Electrochromic Tungsten Oxide Films: Review of Progress 1993–1998. *Sol. Energy Mater. Sol. Cells* **2000**, *60*, 201–262.
- (16) Polaczek, A.; Pekala, M.; Obuszko, Z. Magnetic Susceptibility and Thermoelectric Power of Tungsten Intermediary Oxides. *J. Phys.: Condens. Matter* **1994**, *6*, 7909–7919.
- (17) Balaji, S.; Djaoued, Y.; Albert, A.-S.; Ferguson, R. Z.; Brüning, R. Hexagonal Tungsten Oxide Based Electrochromic Devices: Spectroscopic Evidence for the Li Ion Occupancy of Four-Coordinated Square Windows. *Chem. Mater.* **2009**, *21*, 1381–1389.
- (18) Evans, R. C.; Ellingworth, A.; Cashen, C. J.; Weinberger, C. R.; Sambur, J. B. Influence of Single-Nanoparticle Electrochromic Dynamics on the Durability and Speed of Smart Windows. *Proc. Natl. Acad. Sci. U. S. A.* **2019**, *116*, 12666–12671.
- (19) Hibino, M.; Han, W.; Kudo, T. Electrochemical Lithium Intercalation into a Hexagonal WO<sub>3</sub> Framework and Its Structural Change. *Solid State Ionics* **2000**, *135*, 61–69.
- (20) Mattox, T. M.; Bergerud, A.; Agrawal, A.; Milliron, D. J. Influence of Shape on the Surface Plasmon Resonance of Tungsten Bronze Nanocrystals. *Chem. Mater.* **2014**, *26*, 1779–1784.
- (21) Lee, K.; Seo, W. S.; Park, J. T. Synthesis and Optical Properties of Colloidal Tungsten Oxide Nanorods. *J. Am. Chem. Soc.* **2003**, *125*, 3408–3409.
- (22) Salje, E.; Güttler, B. Anderson Transition and Intermediate Polaron Formation in  $WO_{3-x}$  Transport Properties and Optical Absorption. *Philos. Mag. B* **1984**, *50*, 607–620.
- (23) Salje, E. Polarons and bipolarons in tungsten oxide, WO<sub>3-x</sub>. Eur. J. Solid State Inorg. Chem. **1994**, 31, 805–821.
- (24) Sun, W.; Yeung, M. T.; Lech, A. T.; Lin, C.-W.; Lee, C.; Li, T.; Duan, X.; Zhou, J.; Kaner, R. B. High Surface Area Tunnels in Hexagonal WO<sub>3</sub>. *Nano Lett.* **2015**, *15*, 4834–4838.
- (25) Chen, Z.; Peng, Y.; Liu, F.; Le, Z.; Zhu, J.; Shen, G.; Zhang, D.; Wen, M.; Xiao, S.; Liu, C.-P.; et al. Hierarchical Nanostructured WO<sub>3</sub> with Biomimetic Proton Channels and Mixed Ionic-Electronic Conductivity for Electrochemical Energy Storage. *Nano Lett.* **2015**, 15, 6802–6808.
- (26) Park, S. Y.; Lee, J. M.; Noh, C.; Son, S. U. Colloidal Approach for Tungsten Oxide Nanorod-Based Electrochromic Systems with Highly Improved Response Times and Color Efficiencies. *J. Mater. Chem.* **2009**, *19*, 7959–7964.
- (27) Cabezas, C. A. S.; Ong, G. K.; Jadrich, R. B.; Lindquist, B. A.; Agrawal, A.; Truskett, T. M.; Milliron, D. J. Gelation of plasmonic

- metal oxide nanocrystals by polymer-induced depletion attractions. *Proc. Natl. Acad. Sci. U. S. A.* **2018**, *115*, 8925–8930.
- (28) Wen, R.-T.; Granqvist, C. G.; Niklasson, G. A. Eliminating Degradation and Uncovering Ion-trapping Dynamics in Electrochromic WO<sub>3</sub> Thin Films. *Nat. Mater.* **2015**, *14*, 996–1001.
- (29) Han, X.; Liu, Y.; Jia, Z.; Chen, Y.-C.; Wan, J.; Weadock, N.; Gaskell, K. J.; Li, T.; Hu, L. Atomic-Layer-Deposition Oxide Nanoglue for Sodium Ion Batteries. *Nano Lett.* **2014**, *14*, 139–147.
- (30) Soto, F. A.; Ma, Y.; Martinez de la Hoz, J. M.; Seminario, J. M.; Balbuena, P. B. Formation and Growth Mechanisms of Solid-Electrolyte Interphase Layers in Rechargeable Batteries. *Chem. Mater.* **2015**, 27, 7990–8000.
- (31) Li, C.-P.; Tenent, R. C.; Dillon, A. C.; Morrish, R. M.; Wolden, C. A. Improved Durability of WO<sub>3</sub> Nanocomposite Films Using Atomic Layer and Vapor Deposited Coatings. *ECS Electrochem. Lett.* **2012**, *1*, H24–H27.
- (32) Wen, R.-T.; Niklasson, G. A.; Granqvist, C. G. Sustainable Rejuvenation of Electrochromic WO<sub>3</sub> Films. *ACS Appl. Mater. Interfaces* **2015**, *7*, 28100–28104.
- (33) Lei, J.; Li, L.; Kostecki, R.; Muller, R.; McLarnon, F. J. Characterization of SEI Layers on LiMn<sub>2</sub>O<sub>4</sub> Cathodes with In-Situ Spectroscopic Ellipsometry. *J. Electrochem. Soc.* **2005**, *152*, A774–A777
- (34) Uchaker, E.; Cao, G. Mesocrystals as Electrode Materials for Lithium-Ion Batteries. *Nano Today* **2014**, *9*, 499–524.
- (35) Liu, D.; Cao, G. Engineering Nanostructured Electrodes and Fabrication of Film Electrodes for Efficient Lithium Ion Intercalation. *Energy Environ. Sci.* **2010**, *3*, 1218–1237.
- (36) Garcia, G.; Buonsanti, R.; Runnerstrom, E. L.; Mendelsberg, R. J.; Llordes, A.; Anders, A.; Richardson, T. J.; Milliron, D. J. Dynamically Modulating the Surface Plasmon Resonance of Doped Semiconductor Nanocrystals. *Nano Lett.* **2011**, *11*, 4415–4420.
- (37) Wondimu, T. H.; Chen, G.-C.; Chen, H.-Y.; Kabtamu, D. M.; Bayeh, A. W.; Wang, K.-C.; Huang, H.-C.; Wang, C.-H. High Catalytic Activity of Oxygen-Vacancy-Rich Tungsten Oxide Nanowires Supported by Nitrogen-Doped Reduced Graphene Oxide for the Hydrogen Evolution Reaction. *J. Mater. Chem. A* **2018**, *6*, 19767—19774.
- (38) Downie, L. E.; Hyatt, S. R.; Dahn, J. R. The Impact of Electrolyte Composition on Parasitic Reactions in Lithium Ion Cells Charged to 4.7 V Determined Using Isothermal Microcalorimetry. *J. Electrochem. Soc.* **2016**, *163*, A35–A42.
- (39) Kumar, H.; Detsi, E.; Abraham, D. P.; Shenoy, V. B. Fundamental Mechanisms of Solvent Decomposition Involved in Solid-Electrolyte Interphase Formation in Sodium Ion Batteries. *Chem. Mater.* **2016**, *28*, 8930–8941.
- (40) Jung, Y. S.; Cavanagh, A. S.; Riley, L. A.; Kang, S.-H.; Dillon, A. C.; Groner, M. D.; George, S. M.; Lee, S.-H. Ultrathin Direct Atomic Layer Deposition on Composite Electrodes for Highly Durable and Safe Li-Ion Batteries. *Adv. Mater.* **2010**, *22*, 2172–2176.
- (41) Han, X.; Liu, Y.; Jia, Z.; Chen, Y.-C.; Wan, J.; Weadock, N.; Gaskell, K. J.; Li, T.; Hu, L. Atomic-Layer-Deposition Oxide Nanoglue for Sodium Ion Batteries. *Nano Lett.* **2014**, *14*, 139–147.
- (42) Jung, S. C.; Kim, H.-J.; Choi, J. W.; Han, Y.-K. Sodium Ion Diffusion in Al<sub>2</sub>O<sub>3</sub>: A Distinct Perspective Compared with Lithium Ion Diffusion. *Nano Lett.* **2014**, *14*, 6559–6563.
- (43) Leung, K.; Qi, Y.; Zavadil, K. R.; Jung, Y. S.; Dillon, A. C.; Cavanagh, A. S.; Lee, S.-H.; George, S. M. Using Atomic Layer Deposition to Hinder Solvent Decomposition in Lithium Ion Batteries: First-Principles Modeling and Experimental Studies. *J. Am. Chem. Soc.* **2011**, *133*, 14741–14754.
- (44) Meng, X.; Yang, X.-Q.; Sun, X. Emerging Applications of Atomic Layer Deposition for Lithium-Ion Battery Studies. *Adv. Mater.* **2012**, 24, 3589–3615.
- (45) Wang, Y.; Kim, J.; Gao, Z.; Zandi, O.; Heo, S.; Banerjee, P.; Milliron, D. J. Disentangling Photochromism and Electrochromism by Blocking Hole Transfer at the Electrolyte Interface. *Chem. Mater.* **2016**, 28, 7198–7202.

- (46) Lee, H. D.; Feng, T.; Yu, L.; Mastrogiovanni, D.; Wan, A.; Gustafsson, T.; Garfunkel, E. Reduction of Native Oxides on GaAs during Atomic Layer Growth of Al<sub>2</sub>O<sub>3</sub>. *Appl. Phys. Lett.* **2009**, *94*, 222108
- (47) Li, W.; Liu, X.; Celio, H.; Smith, P.; Dolocan, A.; Chi, M.; Manthiram, A. Mn versus Al in Layered Oxide Cathodes in Lithium-Ion Batteries: A Comprehensive Evaluation on Long-Term Cyclability. *Adv. Energy Mater.* **2018**, *8*, 1703154.
- (48) Li, W.; Kim, U.-H.; Dolocan, A.; Sun, Y.-K.; Manthiram, A. Formation and Inhibition of Metallic Lithium Microstructures in Lithium Batteries Driven by Chemical Crossover. *ACS Nano* **2017**, *11*, 5853–5863.
- (49) Li, W.; Dolocan, A.; Oh, P.; Celio, H.; Park, S.; Cho, J.; Manthiram, A. Dynamic Behaviour of Interphases and Its Implication on High-Energy-Density Cathode Materials in Lithium-Ion Batteries. *Nat. Commun.* **2017**, *8*, 14589.
- (50) Randin, J.-P. Proton Diffusion in Tungsten Trioxide Thin Films. J. Electrochem. Soc. 1982, 129, 2349–2354.
- (51) Martínez-De la Cruz, A.; Torres-Martínez, L. M.; García-Alvarado, F.; Morán, E.; Alario-Franco, M. A. Sodium Ordering in Na,W<sub>18</sub>O<sub>49</sub>. *J. Solid State Chem.* **2000**, *151*, 220–224.
- (52) Whittingham, M. S.; Huggins, R. A. Transport Properties of Inorganic Bronze. In *Fast Transport in Solids*; Van Gool, W., Ed.; North Holland: Amsterdam, 1973; pp 645.
- (53) Cong, S.; Geng, F.; Zhao, Ž. Tungsten Oxide Materials for Optoelectronic Applications. *Adv. Mater.* **2016**, 28, 10518–10528.
- (54) Ederth, J.; Hoel, A.; Niklasson, G. A.; Granqvist, C. G. Small Polaron Formation in Porous WO<sub>3-x</sub> Nanoparticle Films. *J. Appl. Phys.* **2004**, *96*, 5722–5726.
- (55) Niklasson, G. A.; Berggren, L.; Larsson, A.-L. Electrochromic Tungsten Oxide: The Role of Defects. *Sol. Energy Mater. Sol. Cells* **2004**, *84*, 315–328.
- (56) Adachi, K.; Asahi, T. Activation of Plasmons and Polarons in Solar Control Cesium Tungsten Bronze and Reduced Tungsten Oxide Nanoparticles. *J. Mater. Res.* **2012**, *27*, 965–970.
- (57) Mitchell, J. B.; Lo, W. C.; Genc, A.; LeBeau, J.; Augustyn, V. Transition from Battery to Pseudocapacitor Behavior via Structural Water in Tungsten Oxide. *Chem. Mater.* **2017**, *29*, 3928–3937.
- (58) Wang, J.; Polleux, J.; Lim, J.; Dunn, B. Pseudocapacitive Contributions to Electrochemical Energy Storage in TiO<sub>2</sub> (Anatase) Nanoparticles. *J. Phys. Chem. C* **2007**, *111*, 14925–14931.